



# CFD-DEM coupled calculation of entrained air and particles movement characteristics during particles flow impacting the wall process

Hongfa Sun<sup>1</sup> · Zeyu Li<sup>1</sup> · Jibo Long<sup>1</sup> · Li Zeng<sup>2</sup>

Received: 7 February 2022 / Accepted: 19 April 2022 / Published online: 20 May 2022  
© The Author(s), under exclusive licence to Springer-Verlag GmbH Germany, part of Springer Nature 2022

## Abstract

The bulk materials loading and unloading process is common in industrial plants. In order to understand the dust generation mechanism, a physical model of the particles flow impacting the wall process was established in this study. The CFD-DEM coupled calculation method is used to study the entrained air flow field and the particles flow motion characteristics. The results show that with the increase of the wall angle, the farther away from the impact point from the position where the entrained air reaches a steady state, the escape outline distance is longer; As the drop height increases, the 'peak' position of the entrained air of the same section moves backward, and the height of the escape outline is higher; As the mass flow increases, the 'peak' value of entrained air velocity gradually decreases, and the height of the escape outline becomes higher. The typical particle energy loss coefficient in the process of particle flow impacting the wall is greatly affected by the wall angle among the three variables. The  $\alpha$  increases from 15° to 75°, the  $\varphi$  increases from 0.19 to 0.74. The research results can provide a theoretical basis for the control of dust emission in industrial plants.

**Keywords** Particles flow · Dust emission · CFD-DEM · Entrained air · Wall inclination angle

## 1 Introduction

Industrial progress is the source of social development. Bulk materials such as coal powder, aluminum powder, and cement occupy a considerable proportion of industrial raw materials. The process of bulk materials loading and unloading is common in industrial production [1]. It includes two stages: the dropping stage (primary dust generation) and the impacting wall stage (secondary dust generation) [2]. In the dropping stage, due to the mutual drag, the particles drive the surrounding air to move with them, and the drive air is called entrained air. Dust (inhalable fine particles) is difficult to settle in the air by gravity, and it easily escape to the surrounding with the entrained air. The fugitive dust accumulated in the industrial plant seriously polluted the production environment and endangered the physical and mental health of the first-line workers [3, 4].

The ventilation manual clearly states that the reduce dust escape requires to the control entrained air volume [5]. In the 1960s, Hemeon [6] pioneered to study the particles flow free fall process, and proposed a single particle falling model under the action of gravity to predict the entrained air volume. Because of the single particle model has great limitations in practical applications, Tooker [7] modified Hemeon's theory and introduced new parameters to calculate the entrained air volume. Arnold and Cooper [8, 9] conducted further studies on entrained air volume, and found that the cross-sectional area of the particles flow core area is decreases with the drop height increase, while the radius of the boundary layer is increases with the drop height increase. Ullmann [10] analyzed the forces on air and particles based on Hemeon's research, simplified the particles flow falling process to a completely turbulent state, and established a new equation for entrained air volume. Ogata [16, 17] conducted an experimental study on the glass beads falling process, and proposed a entrained air model at  $Re_p < 500$ . Uchiyama [13, 14] found that the particle velocity in the particles flow is greater than the a single particle falling velocity, and the entrained air velocity at the axis is the largest. The particle diameter is larger, the entrained air velocity is greater. Liu [15, 16]

✉ Hongfa Sun  
sunhf1212@xtu.edu.cn

<sup>1</sup> College of Civil Engineering and Mechanics, Xiangtan University, Xiangtan 411105, Hunan, China

<sup>2</sup> Wenzhou Industrial Design Institute Co.,LTD, Wenzhou 325000, Zhejiang, China

verified the entrained air formula obtained by Hemeon and Cooper, and based on the finite volume method derived a new entrained air formula by establishing a cylindrical coordinate system during the particles flow falling process. Ansart [17, 18] established a new calculation formula in order to avoid the influence of empirical parameters on the entrained air volume in the particles flow falling process. Hamzeloo [19] analyzed the particle diameter distribution at the transfer point, and through experimental test obtained the characteristics of entrained air caused by the particles flow falling process under different particle diameter. Esmail [20, 21] analyzed the characteristics of the entrained airflow field caused by the particles flow falling process based on the law of volume conservation, and found that the entrained air volume can be calculated by the volume of the cone flow field formed by the particles flow falling process. Li [22, 23] used the product of entrained air velocity and diffusion area to obtain the calculation formula of entrained air volume based on the  $\pi$  theory. Sun [24–26] derived the entrained air volume formulas involving the particles flow initial velocity and the void ratio of the particles flow core area during the free and adherent falling process of the particles flow, and then used the PIV system to test the characteristics of entrained air, and it was found that the entrained air flow field was mainly affected by the larger particles (325–350  $\mu\text{m}$  used in the experiment).

Research on the particles flow impact on the wall, Thornton [27] studied the comparison of different collision numerical models under the particles collision with the wall. Johnson [28] studied the particles flow impacting the inclined surface, and showed different shapes after the impact. Cundall [29] proposed a numerical calculation method that uses Newton's second law and contact model to describe particle motion and collision. For the numerical calculation of gas–solid two-phase flow, commonly used models include TFM, non-slip single-phase flow model, direct numerical simulation and CFD-DEM coupled calculation. Regarding the particles flow impacting the wall process, the CFD-DEM coupling model is widely used that it can well consider the collision between particles, and the collision between particles and the wall.

As mentioned above, the current research on dust generation during bulk materials loading and unloading mainly focuses on the falling stage. Although the collision between particles and the wall is involved, it does not consider its influence on dust generation. Whether the correlation between the two is still unknown. Therefore, it is necessary to conduct in-depth research on the dust generation mechanism of particles flow impacting the wall. The research results can provide a theoretical basis for the control of dust emission during bulk material loading and unloading in actual engineering.

## 2 Materials and methods

### 2.1 DEM-CFD approach

For the numerical modelling of the particles impact the wall, a coupled multiphase Euler–Lagrange CFD-DEM approach was used. For description of the fluid motion, an ANSYS Fluent [30] is used, while Discrete Element Code is employed to solve the respective transport equations for the particle phase. For the organization of the data transfer between CFD and DEM, a two-way coupling is applied, which is explained in detail by Rickelt [31].

#### 2.1.1 Fluid phase modelling

CFD-DEM coupling calculation treats fluid motion as a continuous phase. Therefore, the fluid governing equation is the local average variable of the mass and energy conservation in the calculation unit. Considering that the volume fraction of the study is less than 10%, the void ratio is ignored in the governing equation [31]. The equation is as follows:

$$\frac{\partial \rho_f}{\partial t} + \nabla \cdot (\rho_f u_f) = 0 \quad (1)$$

$$\frac{\partial (\rho_f u_f)}{\partial t} + \nabla \cdot (\rho_f u_f u_f) = -\nabla P + \nabla R_f + \rho_f g + F_{p-f} \quad (2)$$

where  $u_f$ ,  $\rho_f$ ,  $t$ ,  $P$ ,  $F_{p-f}$ ,  $\tau$  and  $g$  stands for fluid velocity, fluid density, time, fluid pressure, interaction force between fluid and particles, stress tensor and gravitational acceleration, respectively.

The interaction force between gas and solid is very complicated. In this research, it can be calculated by the following equation:

$$F_{p-f} = \frac{1}{V_{cell}} \sum_{j=1}^{k_{cell}} f_{p-f,i} \quad (3)$$

where  $f_{p-f,i}$  represents the total fluid force acting on particle  $i$ ,  $k_{cell}$  represents the total number of particles in the CFD cell, and  $V_{cell}$  represents the volume of the CFD unit.

#### 2.1.2 Solid phase modelling

The particles are solved by DEM. The basic idea of DEM is to use Newton's second law and contact model to describe the movement of the particles. The contact model used in this paper is the soft sphere model, and the contact force model is the Hertz-Mindlin non-slip model [32]. Based on Newton's second law, the particle

governing equation is derived. At time  $t$ , the governing equation of the particle translation and rotation in the two-phase flow is:

$$m_i \frac{dv_i}{dt} = f_{p-g,i} + m_i g + \sum_{j=1}^{k_i} (f_{c,ij} + f_{d,ij}) \tag{4}$$

$$I_i \frac{d\omega_i}{dt} = \sum_{j=1}^{k_i} (T_{c,ij} + T_{r,ij}) \tag{5}$$

where  $m_i, I_i, v_i, \omega_i$  is the mass, moment of inertia, translational velocity and rotation velocity of particle  $i$  respectively. The forces involved in the model include the gravitational force of particle  $i$ , the force between particle  $i$  and particle  $j$ , or the force between particle  $i$  and the wall, and the interaction force between particle and fluid. The force between the particles or between the particles and the wall includes the contact force  $f_{p-g,i}$  and the damping force  $f_{d,ij}$ . In this study, in order to simplify the model, the Safman Force, pressure gradient force, buoyancy force and Magnus force are ignored, and the drag force that plays a key role in the movement of the particle flow is retained. The influence of porosity is ignored in the previous fluid control equation, so the drag force model needs to choose a model without porosity-Free Stream drag force model. The torque is composed of two parts, one part is the contact moment  $T_{c,ij}$ , the other part is the rolling friction moment  $T_{r,ij}$ . For spherical particles, the normal contact force cannot produce a moment, and the contact moment is produced by the tangential contact force. The detailed formula is shown in Table 1.

$$C_D = \begin{cases} 24/Re & Re \leq 0.5 \\ 24(1.0 + 0.15Re^{0.687})/Re & 0.5 \leq Re \leq 1000 \\ 0.44 & Re > 1000 \end{cases}$$

where  $\delta_n$  is the amount of normal overlap,  $\delta_t$  is the amount of tangential overlap,  $E^*$  is the equivalent Young's modulus,  $\nu_i$  is the Poisson's ratio of particle  $i$ ,  $R^*$  is the equivalent radius,  $m^*$  is equivalent mass,  $\beta$  is the damping coefficient,

$S_n$  is the normal stiffness,  $S_t$  is the tangential stiffness,  $v_n^{rel}$  is the normal relative velocity,  $v_t^{rel}$  is the tangential relative velocity,  $\mu_r$  is the coefficient of rolling friction,  $\omega_i$  is the angular velocity of the particle,  $v_{p-g}^{rel}$  is the relative velocity of particle-gas,  $d_p$  is particle diameter,  $C_D$  is the drag coefficient,  $e$  is the coefficient of restitution.

### 2.2 Coupling model

Literatures [34–36] show that the numerical solution method of CFD-DEM has been developed and mature. DEM is to simulate a single particle, and CFD is to simulate the flow field based on a calculation unit. In this study, a two-way simulation of fluid and particles is adopted, and the realization path is shown in Fig. 1: at each time step, based on the fluid flow field, DEM will provide information, such as particle position and velocity, to evaluate the volumetric particle–fluid interaction force. CFD will use these data to update the fluid flow field, thereby generating new particle–fluid interaction forces. Combining the generated force into the DEM will generate motion information for a single particle at the next time step. According to this coupling

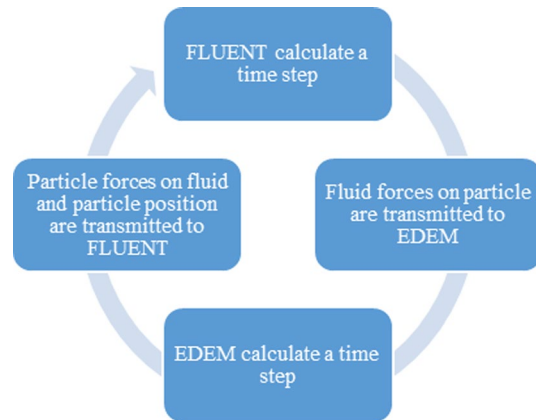


Fig. 1 Coupled computing realization path

Table 1 Force and moment calculation formula

Force and torques	Symbols	Equations
Normal force[33]	Contact	$f_{cn,ij} \quad (4/3)E^*R^{*1/2}\delta_n^{3/2}$
	Damping	$f_{dn,ij} \quad -2(5/6)^{1/2}\beta(S_n m^*)^{1/2}v_n^{rel}$
Tangential forces[33]	Contact	$f_{ct,ij} \quad S_t \delta_t$
	Damping	$f_{dt,ij} \quad -2(5/6)^{1/2}\beta(S_t m^*)^{1/2}v_t^{rel}$
Particle–fluid interaction force	Drag force	$f_{d,i} \quad 0.5C_D \rho_g A  v_{p-g}^{rel}  v_{p-g}^{rel}$
Torque	Rolling fraction	$T_{r,ij} \quad -\mu_r f_{cn,ij} R_i \omega_i$

Where  $\frac{1}{E^*} = \frac{(1-\nu_i^2)}{E_i} + \frac{(1-\nu_j^2)}{E_j}$ ;  $\frac{1}{R^*} = \frac{1}{R_i} + \frac{1}{R_j}$ ;  $\frac{1}{m^*} = \frac{1}{m_i} + \frac{1}{m_j}$ ;  $\beta = \frac{\ln e}{(\ln^2 e + \pi^2)^{1/2}}$ ;  $S_n = 2E^*(R^*\delta_n)^{1/2}$ ;  
 $\frac{1}{G^*} = \frac{(2-\nu_i)}{G_i} + \frac{(2-\nu_j)}{G_j}$ ;  $S_t = 8G^*(R^*\delta_n)^{1/2}$ ;  $A = \pi R^2$ ;  $e = \frac{\rho_g d_p |v_{p-g}^{rel}|}{\eta_g}$ ;  $G_i = E_i/2(1 + \nu_i)$ .

method, the movement of particles, including collisions between particles and between particles and walls, can be well considered for the influence of the flow of the medium.

### 2.3 Numerical setup

This paper selects a space body with a size of  $800\text{ mm} \times 1000\text{ mm} \times h$  as the research object, and its physical model is shown in Fig. 2.  $h$  is the vertical distance from the hopper outlet to the wall.  $\alpha$  is the angle between the wall and the horizontal direction. For the computational grid, we choose a structural grid, and perform local grid refinement on the flow path of the particles flow. For the size of the refined grid, we chose a hexahedral grid with a size of approximately  $5\text{ mm} \times 5\text{ mm} \times 10\text{ mm}$ .

The diameter of bulk material in the actual production process is R-R distribution, and the particle shape is irregular. Yaşar [37] found that the diameter of fine coal ranges from 25 to 500  $\mu\text{m}$ . Luo [38] found that the density of fine coal is between 1300  $\text{kg}/\text{m}^3$  and 1900  $\text{kg}/\text{m}^3$ . Firstly, the entrained air is mainly affected by larger particles, and the small particles have less influence on the entrained air. Second, adopting multiple particle sizes will require more computing time and significantly increase the computing cost. Furthermore, with multi-sized particles, particle segregation is expected and entrained air may become more non-uniform. Finally, the author obtained a median diameter of 335  $\mu\text{m}$  based on the particle size distribution test of fine coal [26]. In this paper, taking fine coal as an example, the particle diameter is 335  $\mu\text{m}$  and the density is 1600  $\text{kg}/\text{m}^3$ . And the shape of the particles set to sphere. The turbulence model selected the K- $\epsilon$  RNG model as following Klemens [39], near-wall processing adopts standard wall functions. Select pressure inlet and pressure outlet for boundary conditions. The impact wall is a smooth and non-slip static wall. For particle–particle and

particle–wall collisions, select the standard Hertz-Mindlin non-slip model to predict. In CFD-DEM simulation, it is very important to determine the appropriate gas–solid time step. The time step of the particle is limited by Rayleigh time [40], which is calculated as Eq. (6). In the actual process, 20% ~ 30% of  $\Delta t_R$  is taken as the time step of the particle phase, and the time step of the liquid phase can be 10 to 100 times that of the particle phase. Detailed boundary conditions is shown in Table 2.

**Table 2** Detailed boundary conditions

Set object	Parameter	Value
Particle phase	Shape	Sphere
	Material	Coal
	Size	335 $\mu\text{m}$
	Density	1600 $\text{kg}/\text{m}^3$
	Particle–particle rolling friction coef	0.05
	Particle–particle static friction coef	0.6
	Particle–particle restitution of coef	0.5
	Shear modulus	$1.1 \times 10^7\text{ Pa}$
	Poisson's ratio	0.23
	Initial velocity	0.5 m/s
Wall	Material	Steel
	Density	7850 $\text{kg}/\text{m}^3$
	Particle–wall rolling friction coef	0.05
	Particle–wall static friction coef	0.4
	Particle–wall restitution of coef	0.5
	Shear modulus	$7.9 \times 10^{10}\text{ Pa}$
	Poisson's ratio	0.3
Fluid phase	Air density	1.225 $\text{kg}/\text{m}^3$
	Air viscosity	$1.8 \times 10^{-5}\text{ Pa} \cdot \text{s}$
	Time step	$2 \times 10^{-4}\text{ s}$

**Fig. 2** Physical model

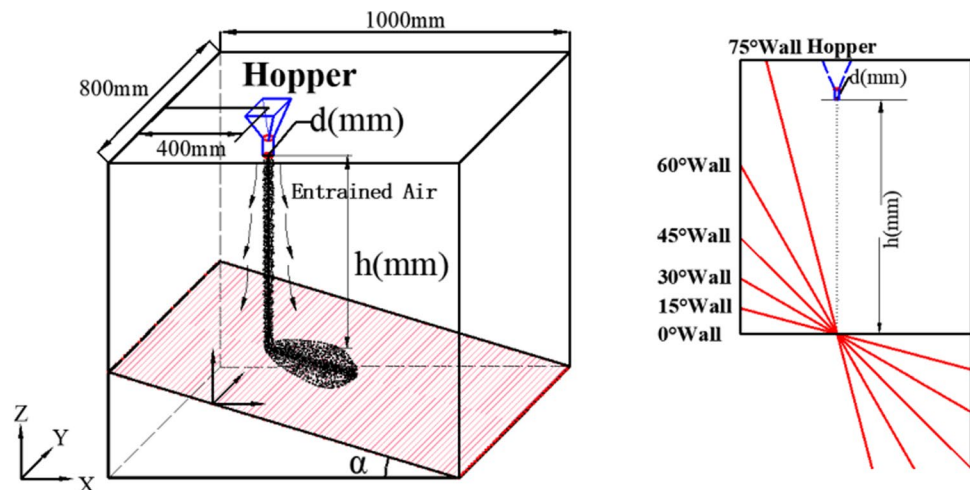


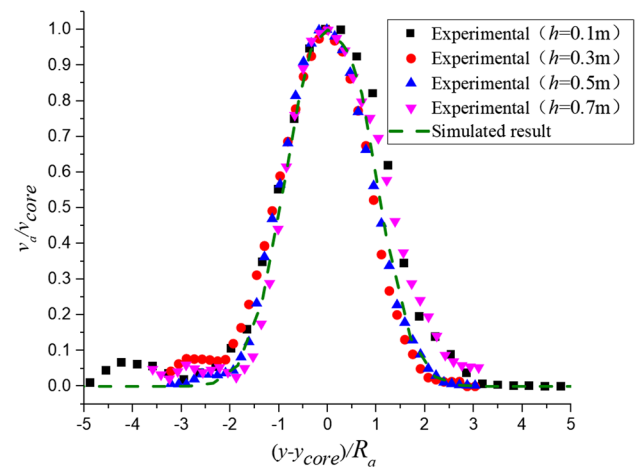
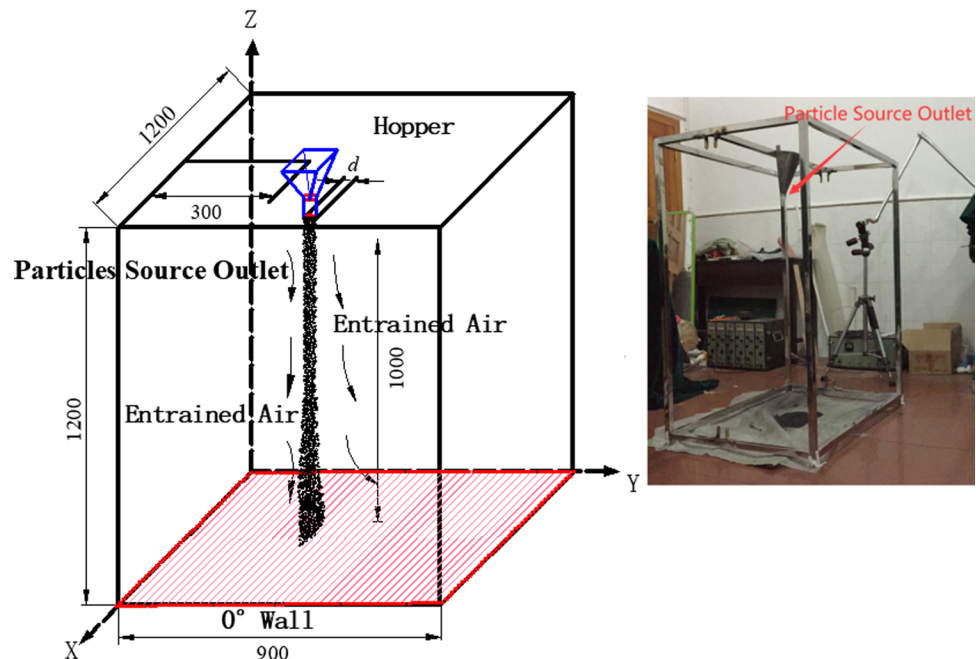
**Table 3** Simulation conditions

Influence parameter	Inclination angle	Drop height	Hopper outlet diameter
Influence of wall inclination angle	15°, 30°, 45°, 60°, 75°	1000 mm	6 mm
Influence of drop height	45°	600 mm, 800 mm, 1000 mm, 1200 mm, 1400 mm	6 mm
Influence of particles flow mass flow	45°	1000 mm	4 mm, 6 mm, 8 mm

$$\Delta t_R = \frac{\pi R_i}{0.1631 v_i + 0.8766} \sqrt{\frac{2 \rho_p (1 + v_i)}{E_i}} \quad (6)$$

$$m_p = 0.583 \rho_b \sqrt{g} (d - 1.4 d_p)^{2.5} \quad (7)$$

In this paper, the numerical simulation conditions are shown in Table 3. The effects of the impact wall inclination angle ( $\alpha$ ), the drop height ( $h$ ) and the hopper outlet diameter ( $d$ ) are studied respectively. For the study of different inclination angles, under the conditions of a height of 1000 mm and hopper outlet diameter of 6 mm, numerical simulations were carried out for five cases of  $\alpha = 15^\circ, 30^\circ, 45^\circ, 60^\circ$  and  $75^\circ$ . For the study of different drop heights, under the condition of an inclination of  $45^\circ$  and a hopper outlet diameter of 6 mm, numerical simulations were carried out for five situations of  $h = 600$  mm, 800 mm, 1000 mm, 1200 mm and 1400 mm. For the study of the influence of different hopper outlet diameters (mass flow), three cases of  $d = 4$  mm, 6 mm and 8 mm were studied under the conditions of an inclination of  $45^\circ$  and a height of 1000 mm. The relationship between hopper outlet diameter and mass flow rate is Eq. (7) [41].

**Fig. 4** Comparison of entrained air velocity simulated between experimental**Fig. 3** The model of simulated and experimental



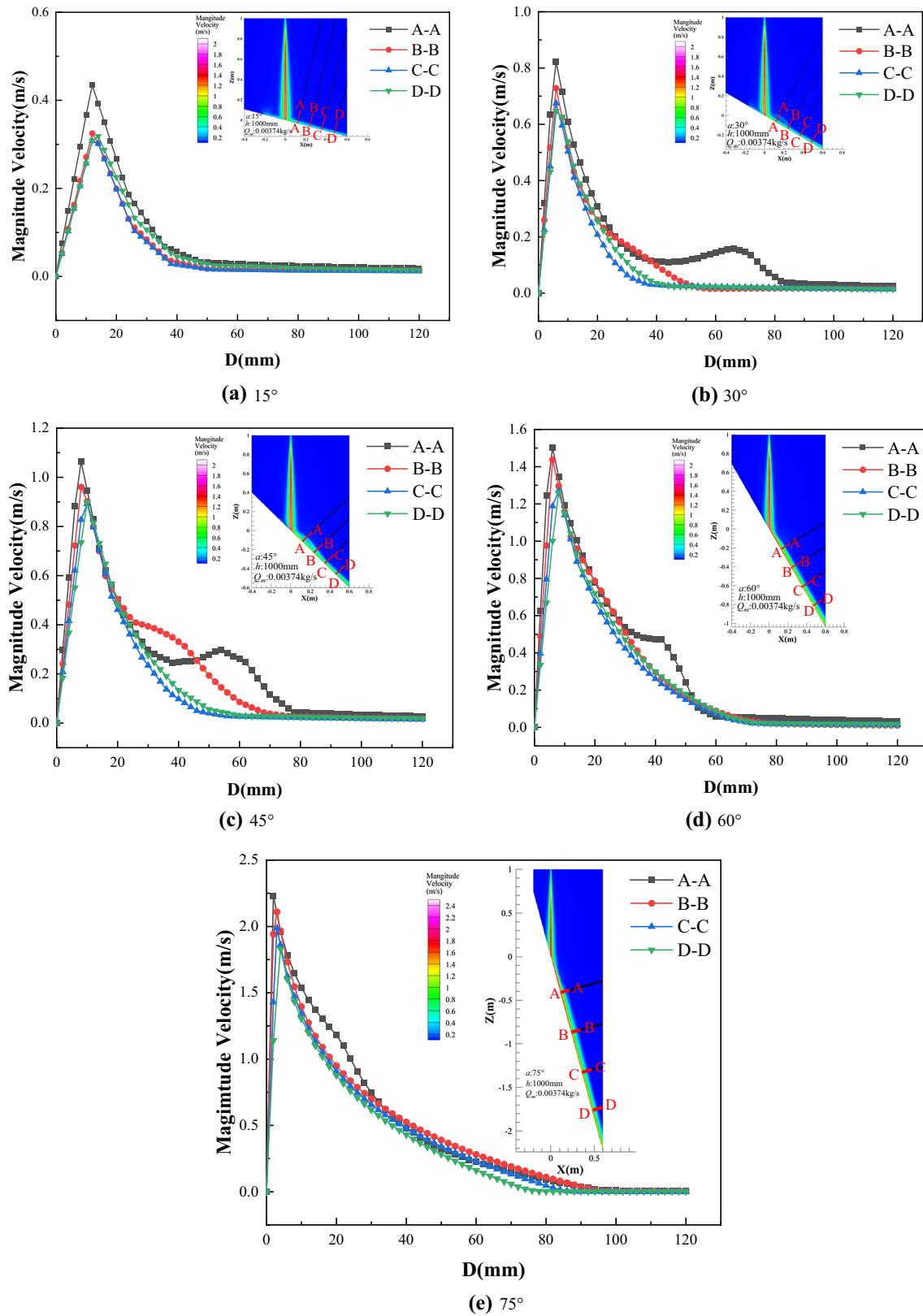
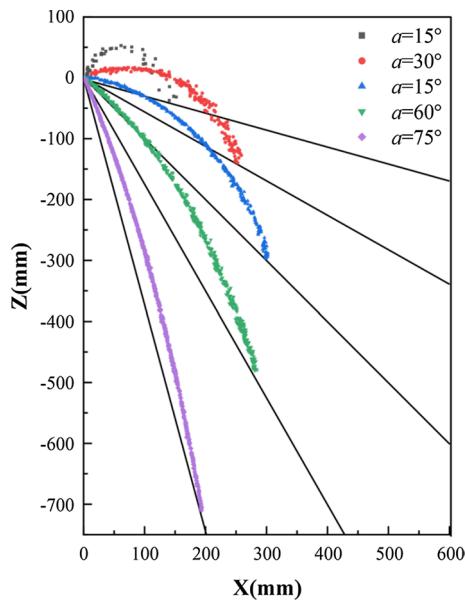
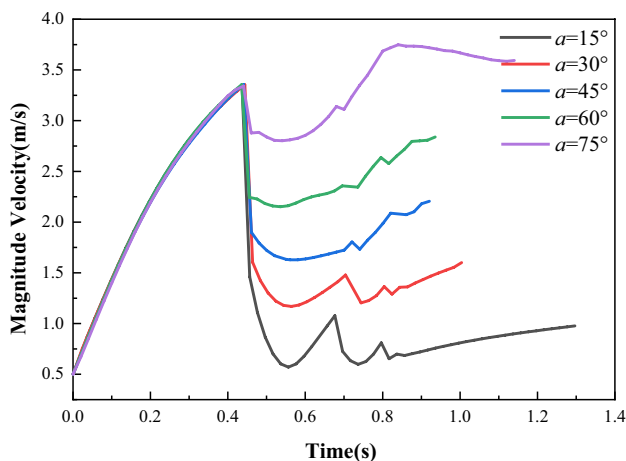


Fig. 5 The influence of wall inclination angles on entrained air in the wall normal direction



**Fig. 6** The influence of wall inclination on the escape outline of particles flow impacting the wall



**Fig. 7** Influence of wall inclination on typical particle velocity

where  $m_p$  is the particles flow mass flow,  $\rho_b$  is the particle bulk density,  $d$  is hopper outlet diameter,  $d_p$  is particle diameter.

## 2.4 Model validation

In order to verify the numerical model, the author used his own experimental compared to the numerical calculation results. The experimental is used the PIV system to test the characteristics of the entrained air flow field caused by the

particles flow vertical fall process [26]. Then use ICEM CFD to establish the corresponding physical model, and choose the numerical calculation method used in this research to calculate the process. The simulation and experimental models are shown in Fig. 3.

As shown in Fig. 4, the experimental entrained air velocity on the four sections of  $h = 0.1$  m, 0.3 m, 0.5 m, 0.7 m and numerical calculation results are dimensionlessly processed. The ordinates is  $v_a/v_{core}$ .  $v_a$  is the entrained air velocity at different positions.  $v_{core}$  is the entrained air maximum velocity at different heights. The abscissa is  $(y-y_{core})/R_a$ .  $y$  is the different positions at different heights.  $y_{core}$  is the particle flow core positions at different heights.  $R_a$  is the entrained air radius at different heights. It can be seen from Fig. 4 that the experimental results and the numerical calculation results are in good agreement.

## 3 Results and discussion

### 3.1 Influence of wall inclination angles

In order to understand the influence of wall inclination angles on the entrained air and the particles flow movement characteristics, five different angles of  $\alpha = 15^\circ$ ,  $30^\circ$ ,  $45^\circ$ ,  $60^\circ$  and  $75^\circ$  were studied in this paper.

The condition of the entrained air flow field selects the velocity distribution on four different sections along the wall normal direction (A–A, B–B, C–C, D–D). As shown in Fig. 5, the entrained air velocity distribution along the wall surface normal direction under different angles. When the angle is constant, the section A–A to D–D the entrained air velocity distribution along the the wall normal direction is roughly Gaussian. The entrained air velocity close to the wall increases sharply due to the existence of the boundary layer, and then decreases sharply as the distance from the wall increases. In addition, it can be seen from Fig. 5 b–d that the ‘peak’ of entrained air velocity fluctuation appears during the decrease of the entrained air velocity in the wall normal direction. The reason for the ‘peak’ is that the particles flow collides with the wall for the first time and then collides with the wall again.

The phenomenon of two ‘peak’ in Fig. 5c is caused by three collisions between the particles flow and the wall. It can be seen from Fig. 5a that when the wall inclination is  $15^\circ$ , there is no second ‘peak’ in the wall normal direction. The reason no ‘peak’ phenomenon is that the wall incident angle is small, the particles flow shadowing effect has a greater impact, and there are fewer particles that cause rebound, and the influence on the entrained air velocity in the wall normal direction can be ignored.

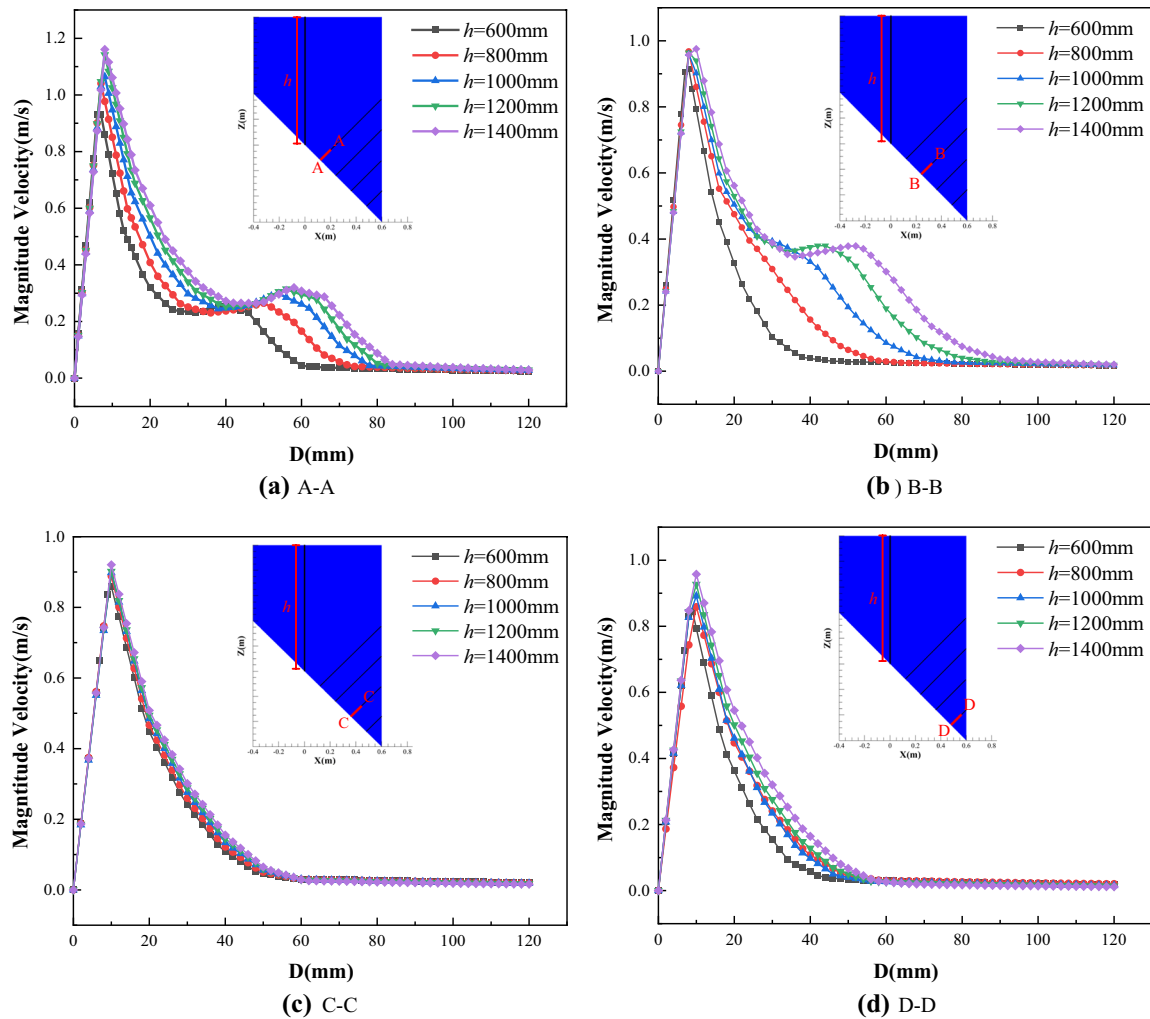


**Fig. 8** The influence of drop height angles on entrained air in the wall normal direction

It can be seen from Fig. 5e that when the wall inclination angle is  $75^\circ$ , the ‘peak’ position appears closer to the maximum entrained air velocity position, because the rebounding particles are closer to the wall. At the same section, as the wall inclination increases, the maximum entrained air velocity also increases. The position of the maximum velocity is closer to the wall as the angle increases (the thickness of the boundary layer is smaller).

From section A-A to D-D, the maximum entrained air velocity gradually decreases. In addition, due to the difference in angles, there has been a phenomenon that it remains unchanged after being reduced to a certain value. The entrained air maximum value is positively correlated with the forces experienced by the particles in the motion of the gas–solid two-phase flow, including gravity, the interaction force between the particles, and the force between the fluid and the particles. After the particles flow impacts the wall, the entrained air velocity is increased by the impact force between the particles and the wall.

The escape outline is the profile of the rebounding portion of the particle flow with the highest concentration in space after the particle flow impacts the wall. As shown in Fig. 6, the particles flow escape outline presents a parabolic distribution under different wall inclination angles. The angle has a greater influence on the particles flow escape outline. As the angle increases, the distance between the first impact point and the second impact point gradually increases. The height of the particles flow escape outline gradually decreases with the increase of the angle. The angle between the particles flow escape outline and the wall normal direction gradually increases with the increase of the angle. From the gas–solid two-phase flow, it can be seen that the entrained air spatial distribution is related to the particles flow spatial distribution, so the particles flow distribution along the wall can well reveal the entrained air velocity distribution.

It can be seen from Fig. 7 that under different wall inclination angles, the typical particle velocity remains



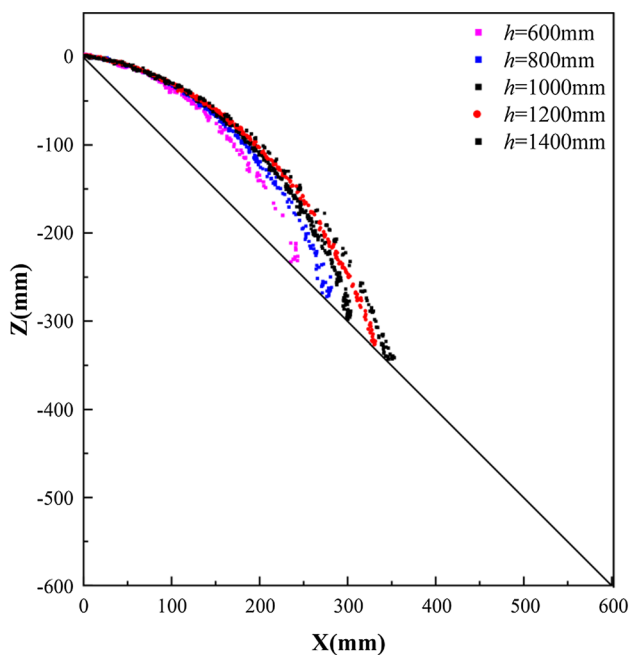


**Fig. 9** The influence of drop height on the escape outline of particles flow impacting the wall

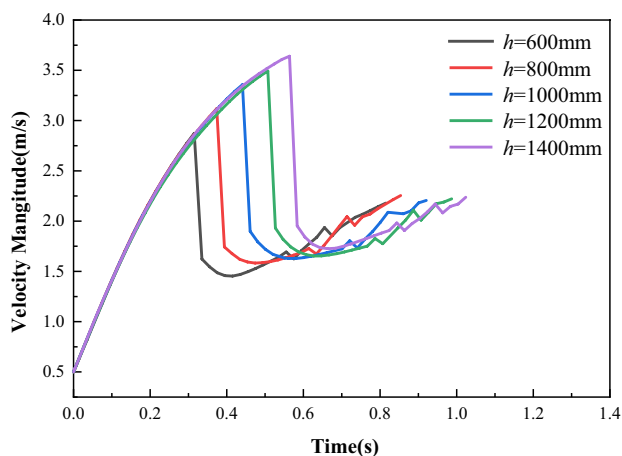


**Fig. 10** Influence of drop height on typical particle velocity

the same before it impacts the wall for the first time. However, the velocity changes greatly after the first impact on the wall. The main reason is that the energy loss during the impact of typical particle with wall of different angles is different. In order to describe the energy loss in the process of particle impacts the wall, this study introduces a new dimensionless parameter energy loss coefficient.

The energy loss coefficient is the square of the rebound velocity compared to the square of the velocity before the particle impacts the wall, and the expression is Eq. (8).

$$\varphi = \frac{(v_2^2)}{(v_1^2)} \quad (8)$$

where  $v_1$  is the velocity before the particle impacts the wall,  $v_2$  is the rebound velocity. The value of  $\varphi$  is 0~1. The value is closer to 1, the velocity loss is smaller.

As the angle increases, the energy loss coefficient of the first collision between the typical particle and the wall is gradually increases. The  $\alpha$  increases from  $15^\circ$  to  $75^\circ$ , the  $\varphi$  increases from 0.19 to 0.74, and the increase rate is also increased. After the collision, the rebounding particle velocity changes from gradual decrease to gradual increase. When the particle collides with the wall for the second time, the typical particle energy continues to lose and the velocity decreases again. Then, continue this process until the particles roll down along the wall. The particles velocity gradually increases as they roll on the wall. When  $\alpha = 75^\circ$ , the velocity change of the particle rolling on the wall is opposite to the other angles. The reason is that when the inclination angle of the wall increases to a certain value, the drag force is greater than the component of gravity in the wall direction due to the higher particle velocity. In addition, there is a certain amount of slippage in the normal direction at the position of the particles maximum velocity and the entrained air maximum velocity on the wall.

### 3.2 Influence of drop height

In order to understand the influence of drop height on the entrained air and the particles flow movement characteristics, five drop height of  $h = 600$  mm, 800 mm, 1000 mm, 1200 mm and 1400 mm were studied in this paper.

As shown in Fig. 8, different drop heights entrained air velocity distribution along the wall normal direction on each section. It can be seen from Fig. 8a that the 'peak' phenomenon appears at the A-A section under different drop heights. As the drop height increases, the 'peak' value velocity continues to increase, and the position moves back. It can be seen from Fig. 8b that when  $h = 600$  mm, the entrained air velocity does not appear 'peak' at the B-B section. As the drop height increases, the 'peak' phenomenon becomes more and more obvious. It can be seen that as the drop height increases, the entrained air velocity generated by the particles flow impacting the wall increases significantly. Figure 8c, d have no 'peak' phenomenon, and the entrained air velocity distribution is basically Gaussian. At the same section, as the drop height increases, the maximum entrained air velocity presents an increasing trend.

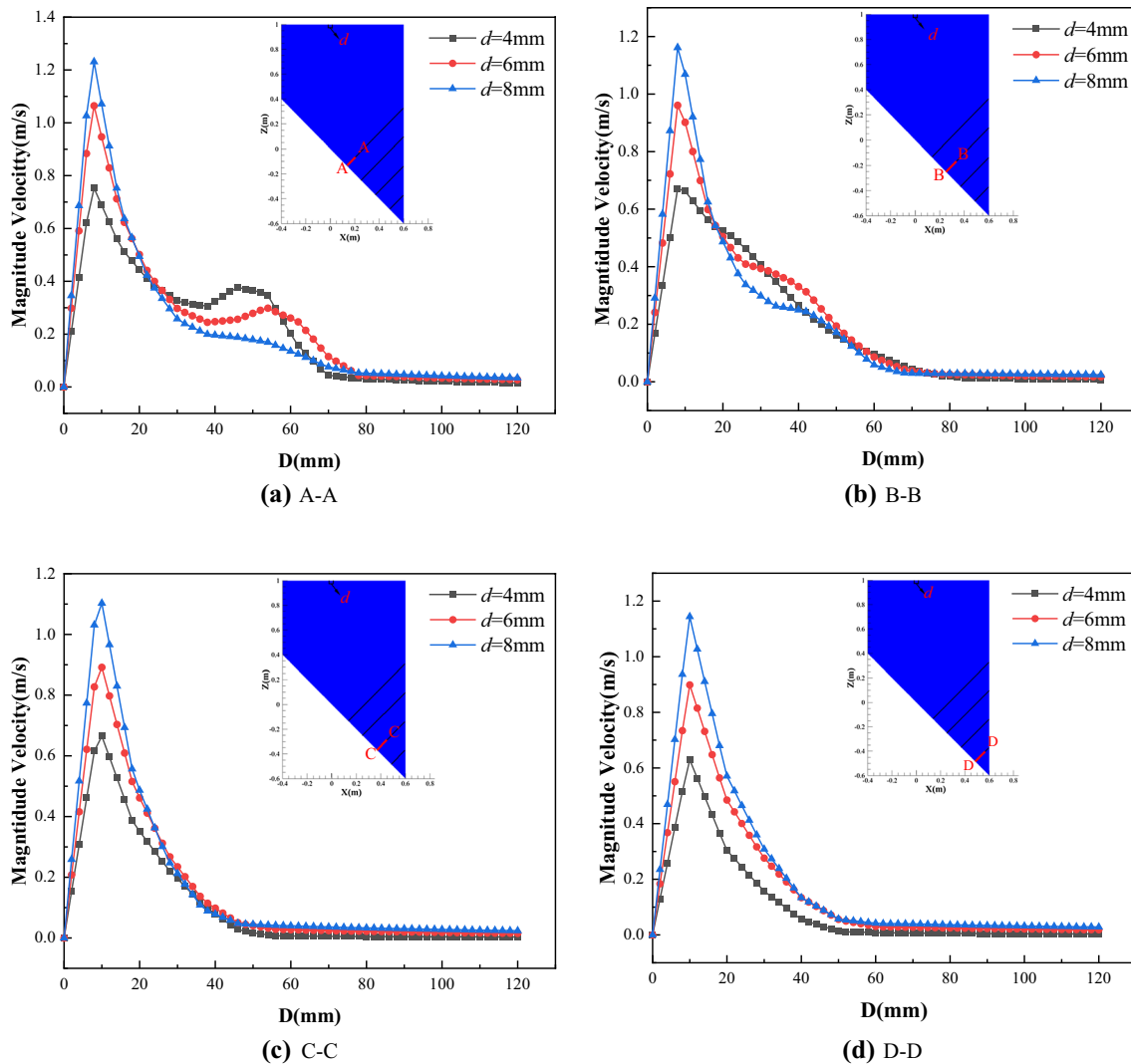


**Fig. 11** The influence of mass flow angles on entrained air in the wall normal direction

As shown in Fig. 9, under different drop heights, the escape outline of the particles flow presents a parabolic distribution. The drop height has little effect on the reflection angle of the particles flow. As the drop height increases, the particles flow escape outline height also increases, and the distance between the first collision point and the second collision point also increases. It can be seen that the drop height has little effect on the dust escape during the particles flow impacting the wall.

As shown in Fig. 10, during the particles flow dropping stage, the variation trend of the typical particle velocity remains the same. When the particle impacts the wall for the first time, the particle energy loss coefficient is approximately equal. It can be seen from Fig. 10 that when the dropping height increases from 600 to 1400 mm, the dropping

time is basically the same for every 200 mm increase in the dropping distance. In practice, as the dropping height increases, the dropping time should gradually decrease for each 200 mm increase in the falling distance. The reason for this phenomenon is that the dropping distance is too short, and the required time difference can be ignored.

### 3.3 Influence of particles flow mass flow

In order to understand the influence of particles flow mass flow on the entrained air and the particles flow movement characteristics, five hopper outlet diameters of  $d=4$  mm, 6 mm and 8 mm were studied in this paper.

Figure 11 shows the entrained air along the wall normal velocity distribution under different mass flow rates.

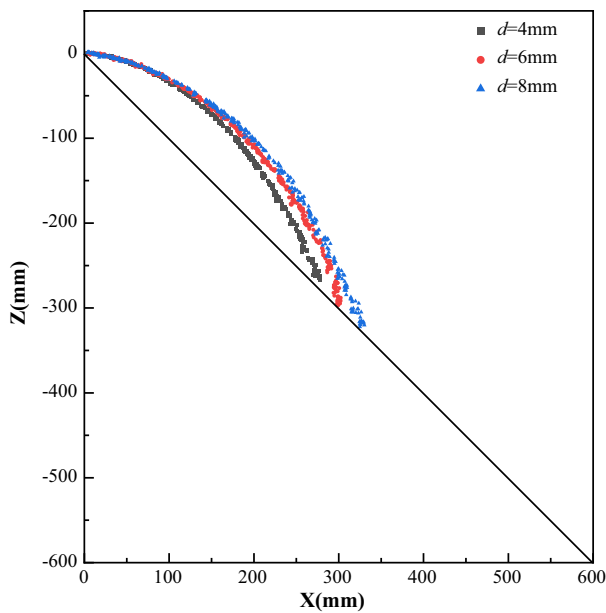


**Fig. 12** The influence of mass flow on the escape outline of particles flow impacting the wall

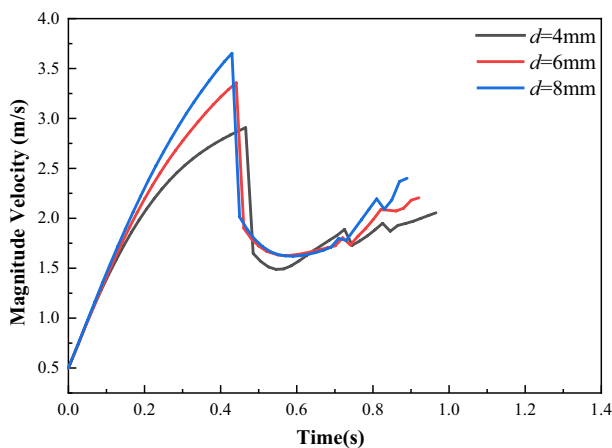


**Fig. 13** Influence of mass flow on typical particle velocity

As shown in Fig. 11a, the entrained air after impacting the wall under different working conditions has a ‘peak’ phenomenon, and the ‘peak’ value gradually decreases with the increase of the mass flow rate. The reason for this phenomenon is that the rebound particles flow is at a position where the velocity is relatively small. As shown in Fig. 11b, when  $d = 4$  mm, there is no obvious ‘peak’ phenomenon. The reason is that the position of the particles flow escape outline is low at the B-B section. As shown in Fig. 11c, d, the entrained air velocity is approximately Gaussian at the C-C and D-D sections. The entrained air velocity increases sharply near the wall due to the presence of the boundary layer, and then gradually decreases as the distance from

the wall increases. With the increase of the hopper outlet diameter, the entrained air velocity under the same section gradually increases, which is consistent with the research of Ogata [12].

As shown in Fig. 12, the particle flow escape outline under different mass flow rates presents a parabolic distribution. As the mass flow increases, the distance between the first impact point and the second impact point gradually increases, and the particles flow escape outline height also gradually increases. The mass flow has little effect on the angle between the particles flow escape outline and the wall normal direction.

Figure 13 shows the effect of mass flow rates on typical particle velocity. In the particles flow dropping stage, the mass flow rate is greater, the particle velocity increases is faster. This phenomenon is consistent with the experimental results of Ogata [12]. When the particles impact the wall for the first time, the particle energy loss coefficients of different mass flow rates are basically the same, which is maintained at 0.3. After the impacting, the particles move along the escape outline, which can be described as a projectile motion with a certain angle and initial velocity. In this process, the particles are affected by the fluid force and the collision force of other particles. The change trend of particle velocity under different mass flow conditions is basically the same.

## 4 Conclusions

This paper takes the particle flow impacting the wall as the research object. After verifying the rationality of the CFD-DEM model, to study the entrained air flow field and the particles flow motion characteristics when the particles flow impacts the wall under different wall inclination angle, drop height, and mass flow.

- The greater the inclination angle of the wall, the weaker the shielding effect of the particles flow and the greater the energy loss coefficient of the particles. The reflection angle and rebound velocity of the particles flow after the first impact on the wall are the main reasons that affect the height of the particles flow escape outline and the position of the second collision point. A phenomenon of ‘peak’ appears on the wall of the entrained air affected by the rebound particles.
- As the drop height and mass flow increase, the velocity of the particles flow before impact on the wall is greater. When the wall inclination angle is constant, the higher the particle velocity after impacting the wall, the higher the height of the particles flow escape outline and the farther the second impact point. The greater the drop height, the greater the ‘peak’ value of entrained air velocity on

the wall. The larger the mass flow, the smaller the ‘peak’ value of entrained air velocity at the wall.

- Through the study of three variables, it is found that the wall inclination angle has the greatest influence on the energy loss coefficient of typical particles. The  $\alpha$  increases from  $15^\circ$  to  $75^\circ$ , the  $\phi$  increases from 0.19 to 0.74. In other words, as the wall inclination angle increases, the dust escape is intensified.

**Acknowledgements** This work was supported by the National Natural Science Foundation of China (Grant No.52108099) and the Excellent Youth Project of Education Bureau of Hunan Province, China (Grant No.21B0134).

## Declarations

**Conflict of interest** The authors declare no conflict of interest.

## References

- Pratap, S., Nayak, A., Kumar, A., Cheikhrouhou, N., Tiwari, M.K.: An integrated decision support system for berth and ship unloader allocation in bulk material handling port[J]. *Comput. Ind. Eng.* **106**, 386–399 (2017)
- Faschingleitner, J., Flinger, W.H.: Evaluation of primary and secondary fugitive dust suppression methods using enclosed water spraying systems at bulk solids handling[J]. *Adv. Powder Technol.* **22**(2), 236–244 (2011)
- Neuman, M.K., Boulton, J.W., Sanderson, S.: Wind tunnel simulation of environmental controls on fugitive dust emissions from mine tailings[J]. *Atmos. Environ.* **43**(3), 520–529 (2009)
- Schulz, D., Schwindt, N., Schmidt, E., Jasevičius, R., Kruggel-Emden, H.: Investigation of the dust release from bulk material undergoing various mechanical processes using a coupled DEM/CFD approach[J]. *Powder Technol.* **355**, 37–56 (2019)
- Sun, Y.: *Concise Ventilation Design Manual*[M]. China Building Industry Press, Beijing (1997)
- Hemeon, W.C.L.: *Plant and Process Ventilation*[M], 1st edn. The Industrial Press, New York (1963)
- Tooker, G.E.: Control fugitive dust emissions in material handling operation[J]. *Bulk solids handling.* **12**(2), 227–232 (1992)
- Cooper, P., Arnold, P.: Air Entrainment and Dust Generation from a Falling Stream of Bulk Material[J]. *Powder & Particle.* **13**, 125–134 (1995)
- Cooper P., Liu Z.Q., Glutz A. (1998) Air Entrainment Processes and Dust Control in Bulk Materials Handling Operations. In: 6th International Conference on Bulk Materials Storage, Handling and Transportation, The University of Wollongong, Australia
- Ullmann, A., Abraham, D.: Exhaust volume model for dust emission control of belt conveyor transfer points[J]. *Powder Technol.* **96**(2), 139–147 (1998)
- Ogata, K., Funatus, K., Tomita, Y.: Entrained air flow characteristics due to the powder jet[J]. *J. Soci Powder Technol Jpn.* **37**(3), 160–167 (2000)
- Ogata, K., Funatsu, K., Tomita, Y.: Experimental investigation of a free falling powder jet and the air entrainment[J]. *Powder Technol.* **115**, 90–95 (2001)
- Uchiyama, T.: Numerical analysis of particulate jet generated by free falling particles[J]. *Powder Technol.* **145**, 123–130 (2004)
- Uchiyama, T., Naruse, M.: Three-dimensional vortex simulation for particulate jet generated by free falling particles[J]. *Chemical Engineer Science.* **61**, 1913–1921 (2006)
- Liu, Z.Q., Wypych, P., Cooper, P.: Dust generation and air entrainment in dust handling—a review[J]. *Powder Handl. Process* **4**(4), 421–425 (1999)
- Liu, Z.Q., Cooper, P., Wypych, P.: Experimental investigation of air entrainment in free-falling particle plumes[J]. *Part. Sci. Technol.* **25**, 357–373 (2007)
- Ansart, R., Ryck, A.D., Dodds, J.A., Roudet, M., Fabre, D., Charru, F.: Dust emission by powder handling: comparison between numerical analysis and experimental results[J]. *Powder Technol.* **190**, 274–281 (2009)
- Ansart, R., Ryck, A.D., Dodds, J.A.: Dust emission in powder handling: free falling particle plume characterization[J]. *Chem. Eng. J.* **152**, 415–420 (2009)
- Hamzeloo, E., Massinaei, M., Mehrshad, N.: Estimation of particle size distribution on an industrial conveyor belt using image analysis and neural networks[J]. *Powder Technol.* **261**, 185–190 (2014)
- Esmaili, A.A., Donohue, T.J., Wheeler, C.A., McBride, W.M., Roberts, A.W.: A new approach for calculating the mass flow rate of entrained air in a freefalling material stream. *Part. Sci. Technol.* **31**(3), 248–255 (2013). <https://doi.org/10.1080/02726351.2012.715617>
- Esmaili, A.A., Donohue, T.J., Wheeler, C.A., Mc Bride, W.M., Roberts, W.A., Donohue, J.T.: On the analysis of a coarse particle free falling material stream[J]. *Int. J. Miner. Process.* **142**, 82–90 (2015)
- Li, X.C., Li, Q., Zhang, D., Jia, B., Luo, H., Hu, Y.: Model for induced airflow velocity of falling materials in semi-closed transfer station based on similitude theory[J]. *Adv. Powder Technol.* **26**, 236–243 (2015)
- Li, X.C., Wang, Q., Li, Q., Hu, Y.: Developments in studies of air entrained by falling dust[J]. *Powder Technol.* **291**, 159–169 (2016)
- Sun, H., Li, A., Jifu, Wu.: Entrained air by particle plume: comparison between theoretical derivation and numerical analysis[J]. *Part. Sci. Technol.* **39**(2), 141–149 (2021)
- Sun, H., Li, A., Jifu, Wu., Zhang, J.: Particle flow fall process: a systematic study of entrained air under unconfined and semi-confined fall conditions[J]. *Granular Matter* **22**, 49 (2020)
- Sun, H., Li, A., Long, J., Jifu, Wu., Zhang, W., Zhang, J.: Experimental study on the characteristics of entrained air during the particle flow fall process[J]. *Powder Technol.* **374**, 421–429 (2020)
- Thornton, C., Cummins, S.J., Cleary, P.W.: An investigation of the comparative behaviour of alternative contact force models during inelastic collisions[J]. *Powder Technol.* **233**, 30–46 (2013)
- Johnson, C.G., Gray, J.M.N.T.: Granular jets and hydraulic jumps on an inclined plane[J]. *J. Fluid Mech.* **675**, 87–116 (2011)
- Cundall, P.A., Strack, O.: A discrete numerical model for granular assemblies[J]. *Géotechnique.* **30**(3), 331–336 (2008)
- Komossa, H., Wirtz, S., Scherer, V., Herz, F., Specht, E.: Transversal bed motion in rotating drums using spherical particles: comparison of experiments with DEM simulations[J]. *Powder Technol.* **264**, 96–104 (2014)
- Rickelt, S., Sudbrock, F., Wirtz, S., Scherer, V.: Coupled DEM/CFD simulation of heat transfer in a generic grate system agitated by bars[J]. *Powder Technol.* **249**, 360–372 (2013)
- Thornton, C., Cummins, S.J., Cleary, P.W.: An investigation of the comparative behaviour of alternative contact force models during elastic collisions[J]. *Powder Technol.* **210**, 189–197 (2011)
- Teng, S., Wang, P., Zhang, Q., Gogos, C.: Analysis of fluid energy mill by gas-solid two-phase flow simulation[J]. *Powder Technol.* **208**, 684–693 (2011)

34. Zhou, M., Wang, S., Kuang, S., Luo, K., Fan, J., Yu, A.: CFD-DEM modelling of hydraulic conveying of solid particles in a vertical pipe[J]. *Powder Technol.* **354**, 893–905 (2019)
35. Zhao, H., Zhao, Y.: CFD-DEM simulation of pneumatic conveying in a horizontal pipe[J]. *Powder Technol.* **373**, 58–72 (2020)
36. Chu, K.W., Wang, Y., Zheng, Q.J., Yu, A.B., Pan, R.H.: CFD-DEM study of air entrainment in falling particle plumes[J]. *Powder Technol.* **361**, 836–848 (2020)
37. Yaşar, Ö., Uslu, T., Şahinoğlu, E.: Fine coal recovery from washery tailings in turkey by oil agglomeration[J]. *Powder Technol.* **327**, 29–42 (2017)
38. Luo, Z., Chen, Q.: Effect of fine coal accumulation on dense phase fluidized bed performance[J]. *Int. J. Miner. Process.* **63**, 217–224 (2001)
39. Klemens, R., Kosinski, P., Wolanski, P., Korobeinikov, V.P., Markov, V.V., Menshov, I.S., Semenov, I.V.: Numerical study of dust lifting in a channel with vertical obstacles[J]. *J. Loss Prev. Process Ind.* **14**, 469–473 (2001)
40. Li, Y., Xu, Y., Thornton, C.: A comparison of discrete element simulations and experiments for “sandpiles” composed of spherical particles[J]. *Powder Technol.* **160**, 219–228 (2005)
41. Fowler, R.T., Glastonbury, J.R.: The flow of granular solids through orifices[J]. *Chem. Eng. Sci.* **10**, 150–156 (1959)

**Publisher's Note** Springer Nature remains neutral with regard to jurisdictional claims in published maps and institutional affiliations.